Coherent structure and heat transfer in geostrophic flow under density stratification

O. Iida and Y. Nagano
Department of Mechanical Engineering, Nagoya Institute of Technology, Gokiso-cho, Showa-ku, Nagoya 466-8555, Japan

(Received 21 April 1997; accepted 30 October 1998)

The mechanism of heat transport in geostrophic flows under various density stratifications has been studied by using both direct numerical simulation and rapid distortion theory. It is found that in cases with rotation, the iso-surfaces of the temperature fluctuations are aligned in the direction of the rotational axis, and they become very close to two-dimensional. Under stable stratification with rotation, the velocity and temperature fluctuations tend to oscillate with the Brunt–Väisälä frequency, while they tend to oscillate with a longer period in cases without rotation. Under unstable stratification with rotation, on the other hand, vortex columns are formed in the direction parallel to the axis of rotation owing to the effects of nonlinear interactions. © *1999 American Institute of Physics.* [S1070-6631(99)02702-6]

I. INTRODUCTION

In geophysically and astrophysically important flows, two kinds of body forces, i.e., the buoyancy and Coriolis forces, are simultaneously imposed. Recently, increasing attention has been paid to their mixed effects on turbulence to resolve planetary circulation issues.

The density stratification associated with the buoyancy force can be classified into two categories, i.e., stable stratification and unstable stratification. The mixed effects of the Coriolis force and the unstable stratification on turbulence are studied mainly on the convection problem observed in wall-bounded flows.[1–8] The flow pattern of Rayleigh–Bénard convection under rotation can be classified approximately by the both Rayleigh number and the Taylor number. The experiments of Boubnov and Golitsyn,[4,5] Fernando *et al.*,[6,7] and Sakai[8] have been performed at a sufficiently high value of Rayleigh and Taylor number to generate turbulent convection. When the Rayleigh number is below the critical value, the fluid is at rest and heat transport is accomplished by thermal conductivity. This critical Rayleigh number is the minimum Rayleigh number required for the onset of convection, and was first found as a function of the Taylor number by Nakagawa and Frenzen.[1] However, even beyond this critical Rayleigh number typical Rayleigh–Bénard convection does not appear when imposed rotation is sufficiently large, while thin elongated vortex columns with a vertical axis are generated between the two walls. It is also found that the horizontal scale of these vortex columns becomes small as the Rossby number decreases, while their vertical scale increases and more intense isolated vortex columns can be observed. Almost all these vortex columns are cyclonic, which cannot be explained sufficiently in these experiments.

Direct numerical simulations and large eddy simulations of the rotating Rayleigh–Bénard convection have been carried out by Raash and Etling,[9] Cabot *et al.*,[10] and Julien *et al.*[11,12] Their results were qualitatively in good agreement with the previous experiments, although exact comparisons were not possible due to different values for the Rayleigh, the Taylor, and the Prandtl number. In both the numerical studies of Cabot *et al.*[10] and Julien *et al.*,[11,12] two kinds of surface boundary conditions, i.e., nonslip and free-slip walls, were imposed on the channel, and the effects of wall boundary condition on vortex columns and heat transfer associated with them were discussed in detail. Julien *et al.*[12] found that the vortex columns became cyclonic in the process in which stationary fluid was ejected toward the central region of a channel by buoyancy, and the vorticity in the generated plume was intensified by the vortex stretching associated with the horizontal convergence of the flow. However, it is still unknown how the buoyancy force, Coriolis force, and especially the nonlinear term affect their generation, respectively.

The generation mechanism of vortex columns was also studied by the experiments and numerical simulation of injecting dense saltwater into a rotating water tank.[13–15] The saltwater sank into the underlying less-dense homogeneous water forming a growing three-dimensional (3D) turbulent layer. When the turbulent front reached a transition depth, the Coriolis force affected turbulence and quasi-2D vortex structures were generated beneath the 3D turbulent mixed layer. These vortices then penetrated downward to produce vortex columns and eventually occupied the rest of the tank beneath the upper mixed layer. In these previous experiments, the parameters governing the characteristic length and velocity scale of the vortex columns were determined.

The vortex columns are closely associated with the dust-devil observed in the lower atmosphere near the ground[7] and the oceanic vortices associated with hydrothermal plumes.[16] Hence, the rotating turbulence under unstable stratification is important, especially in the geophysical flows. Unfortunately, all of these studies were conducted on wall-bounded flows, whereas there are none for the homogeneous turbulence which is equally important in the geophysical flow. In

 © 1999 American Institute of Physics

Downloaded 06 Sep 2010 to 133.68.192.96. Redistribution subject to AIP license or copyright; see http://pof.aip.org/about/rights_and_permissions

TABLE I. Computational conditions. In the table, N_g represents the number of grid points.

Case	N	NR1	NR2	S	SR1	SR2	SR3	SR4	SR5	SR6	SR7
N_g	32^3										
ν	0.0243										
Pr ($\equiv \nu/\alpha$)	0.71		10				0.71				
S_θ	1										
$g\beta$	0	0	0	4	4	1	4	1	4	16	4
Ω	0	10		0	10	5	20	10	5	10	10
S ($\equiv \sqrt{\lvert g\beta S_\theta \rvert}/2\Omega$)	0.1			0.05			0.2			0.1	

Case	U	UR1	UR2	UR3	UR4	UR5	UR6	UR7	UR8	UR9	UR10	UR11	UR12
N_g	32^3									64^3			
ν	0.0243									0.012			
Pr	0.71												
S_θ	-1												
$g\beta$	4	4	1	4	1	4	16	4	1	4	1	4	16
Ω	0	10	5	20	10	5	10	10	5	20	10	5	10
S	0.1		0.05		0.2		0.1		0.05		0.2		

homogeneous turbulence, it is possible to investigate the generation mechanism of vortex columns by expansion of velocity fluctuations into Fourier spectra in all directions.

Homogeneous turbulence has been used as an objective flow field, although to the authors' knowledge there is no previous DNS study on rotational homogeneous turbulence under unstable stratification. The effect of rotation has been successfully demonstrated in the studies on homogeneous turbulence without buoyancy.[17–21] All these numerical simulations and experiments showed a quasi-two dimensionalization, where integral-length scale increased in the direction parallel to the rotational axis. However, no study has ever noted the marked tendency for the velocity vector to align itself perpendicular to the rotational axis, as predicted by the Taylor–Proudmann theorem. Another remarkable feature is that the rotation reduces the nonlinear triad interaction and the energy cascade of turbulence. Thus, turbulent kinetic energy is piled up at low-wave numbers, while high-wave-number energy decreases markedly. The experiment of Komori *et al.*[22] showed that under unstable stratification, turbulence activity was enhanced over all wave numbers and the energy cascade. Hence, the effects of rotation and stratification are in conflict with each other.

We also study the effects of rotation on stably stratified turbulence. The most important feature in the stably stratified flow should be the occurrence of the internal gravity wave. Previously, the effects of rotation on stably stratified turbulence has been mainly studied with the geostrophically approximated equation, where the internal gravity waves were removed by the hydrostatic assumption along the vertical axis.[23–25] Metais *et al.*[26] carried out three-dimensional numerical simulations of strongly stratified and rotating turbulence. However, we have little knowledge about the effects of solid rotation on the internal gravity wave excluding the theoretical works.[25,27]

Our main objective in the present study is to numerically investigate the effects of solid body rotation on both stably and unstably stratified turbulence. The three-dimensional Navier–Stokes equation with the Boussinesq approximation is solved, and the coherent structures and heat transfer in geostrophic flows are studied in detail.

II. NUMERICAL PROCEDURE

All computations are carried out in the domain of a cubic box of which sides are set to be 2π, and periodic boundary conditions are assumed on each side. The cubic box is also assumed to rotate around the x_3 axis. Both the mean temperature gradient ($S_\theta \equiv d\Theta/dx_3$) and the gravitational acceleration g are imposed in the x_3 direction.

The parameters included in the governing equations are kinematic viscosity ν, thermal diffusivity α, angular velocity Ω, and buoyancy parameter $g\beta$, where β represents the volume expansion rate. The typical values studied are listed in Table I. In this table, neutrally stratified cases are designated by an N, and stably and unstably stratified cases are represented by S and U, respectively, while rotation is designated by a following R. Because the gravitational acceleration g is imposed in the downward direction, the negative mean temperature gradient indicates the unstable stratification, while the positive gradient makes the flow field stable in the dynamical sense. In all stratified cases with rotation, i.e., Case NR1, SR1, and UR1, the rapid distortion theory (RDT) is applied as well as the direct numerical simulations. From Case N to UR6 listed in Table I, the same energy spectrum (ES1) is used as the initial condition, while from Case UR7 to UR12 the other initial energy spectrum (ES2) is used. The energy spectra ES1 and ES2 are defined in the following:

$$\mathrm{ES1}(\kappa_1,\kappa_2,\kappa_3) = 0.018\kappa^2 \exp\left(-\frac{\kappa^2}{25}\right), \tag{1}$$

$$\mathrm{ES2}(\kappa_1,\kappa_2,\kappa_3) = 0.18\kappa \exp\left(-\frac{\kappa}{3}\right),$$

$$\mathrm{ES2}(\kappa_1,\kappa_2,0) = 0. \tag{2}$$

In the above equation, κ_i represents the wave number in the i-th direction, while κ is the three-dimensional wave number. In the energy spectrum ES2, the velocity fluctuations at κ_3

Downloaded 06 Sep 2010 to 133.68.192.96. Redistribution subject to AIP license or copyright; see http://pof.aip.org/about/rights_and_permissions

$=0$ are set to be zero, indicating that there is no integral scale in the x_3 direction. It should be noted that without the initial integral scale, RDT cannot predict any evolution of velocity fluctuations of $\kappa_3=0$.

The numerical procedure is based on the pseudo-spectral method where the governing equations are discretized by the Fourier-collocation method. The maximum number of grid points used in the study is 64^3. The second-order Runge–Kutta method is used for the time integration. The initial condition of the velocity field is artificially generated isotropic turbulence without any temperature fluctuation except Case SR7. Temperature fluctuations are generated spontaneously by turbulence activity under the imposed mean temperature gradient. In Case SR7, however, artificially generated temperature fluctuations are assumed as the initial condition.

The Boussinesq-approximated Navier–Stokes equation, the continuity equation, and the equation of temperature fluctuation θ take the following forms when nondimensionalized by the appropriate length scale L, the velocity scale U, and the temperature scale ΔT $(\equiv|S_\theta|L)$:

$$\frac{\partial u_i}{\partial t}+u_j\frac{\partial u_i}{\partial x_j}=-\frac{\partial p}{\partial x_i}+\frac{1}{\mathrm{Re}}\frac{\partial^2 u_i}{\partial x_j\partial x_j}-\frac{1}{\mathrm{Ro}}(-u_2\delta_{i1}+u_1\delta_{i2})+\frac{\theta}{\mathrm{Bo}}\delta_{i3}, \tag{3}$$

$$\frac{\partial u_i}{\partial x_i}=0, \tag{4}$$

$$\frac{\partial \theta}{\partial t}+u_j\frac{\partial \theta}{\partial x_j}=-u_3+\frac{1}{\mathrm{Re\,Pr}}\frac{\partial^2\theta}{\partial x_j\partial x_j}, \tag{5}$$

where $\mathrm{Re}=UL/\nu$, $\mathrm{Ro}=U/(2\Omega L)$, and $\mathrm{Bo}=U^2/(Lg\beta\Delta T)$ are the Reynolds number, the Rossby number, and the buoyancy parameter, respectively. Also, u_i and p are the i-th component of the velocity vector and pressure, respectively. The ratio of the viscosity to the Coriolis force results in the Ekman number $\mathrm{Ek}=\nu/(2\Omega L^2)$. When the square root of the turbulent kinetic energy $\sqrt{k}$ and the characteristic length scale of turbulence $k^{3/2}/\epsilon$ are used as the reference scales, these parameters become $\mathrm{Re}=k^2/\epsilon\nu$, $\mathrm{Ro}=\epsilon/(2\Omega k)$, $\mathrm{Bo}=\epsilon/(\sqrt{k}g\beta\Delta T)$, $\mathrm{Ek}=\nu\epsilon^2/(2\Omega k^3)$, respectively. In all cases except the unstable stratification, the Reynolds number is below 20. In the most complex case of unstable stratification with rotation, the Reynolds number begins to increase markedly just after vortex columns are generated, as discussed later. However, our dominant objective is to investigate the generation mechanism of vortex columns, which begins at relatively low-Reynolds numbers. Both the Rossby and the Ekman numbers are around 0.1 in all cases. Thus, all the flow fields become geostrophic flow, where the balance between the pressure and the Coriolis force is retained.

III. RESULTS AND DISCUSSION

A. Cases of neutral and stable stratification

Figure 1 shows the distribution of the temperature fluctuations and the velocity vectors in the x_1-x_3 plane in the neutrally stratified case with rotation. It becomes evident that the iso-surfaces of the temperature fluctuations are aligned in the direction parallel to the axis of the rotation, indicating that the temperature field becomes two-dimensional when solid body rotation is imposed.

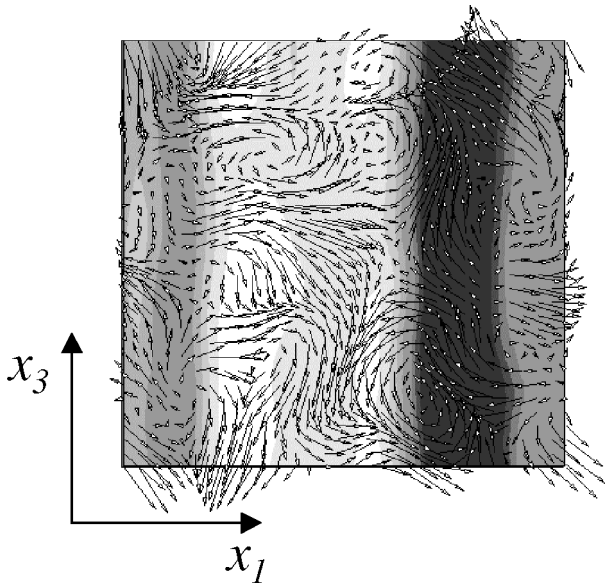

FIG. 1. The distribution of temperature fluctuations and velocity vectors in the x_1-x_3 plane (Case NR1): Black to white; -0.5 to 0.5, $t=2.0$.

The effects of rotation on temperature fluctuations are studied through RDT. By neglecting both the nonlinear and viscous terms, the following solutions are obtained analytically for the Fourier spectrum of the velocity and temperature, i.e., $\hat{u}_i$, $\hat{\theta}$:

$$\boldsymbol{\kappa}=(\kappa_1,\kappa_2,\kappa_3). \tag{6}$$

When $\kappa_3\neq 0$,

$$\begin{aligned}
\hat{u}_1(\boldsymbol{\kappa},t)&=\hat{u}_1(\boldsymbol{\kappa},0)\cos\gamma t+\{\eta\hat{u}_1(\boldsymbol{\kappa},0)+\zeta\hat{u}_2(\boldsymbol{\kappa},0)\}\sin\gamma t,\\
\hat{u}_2(\boldsymbol{\kappa},t)&=\hat{u}_2(\boldsymbol{\kappa},0)\cos\gamma t-\{\xi\hat{u}_1(\boldsymbol{\kappa},0)+\eta\hat{u}_2(\boldsymbol{\kappa},0)\}\sin\gamma t,\\
\hat{u}_3(\boldsymbol{\kappa},t)&=\hat{u}_3(\boldsymbol{\kappa},0)\cos\gamma t+\left(\frac{1}{\kappa}\right)\{\kappa_2\hat{u}_1(\boldsymbol{\kappa},0)-\kappa_1\hat{u}_2(\boldsymbol{\kappa},0)\}\sin\gamma t,\\
\hat{\theta}(\boldsymbol{\kappa},t)&=\frac{1}{2\Omega\kappa_3}S_\theta\times[\kappa_2\{\hat{u}_1(\boldsymbol{\kappa},t)-\hat{u}_1(\boldsymbol{\kappa},0)\}-\kappa_1\{\hat{u}_2(\boldsymbol{\kappa},t)-\hat{u}_2(\boldsymbol{\kappa},0)\}]+\hat{\theta}(\boldsymbol{\kappa},0),
\end{aligned} \tag{7}$$

with

$$\gamma=2\Omega\frac{\kappa_3}{\kappa},\quad \eta=\frac{\kappa_1\kappa_2}{\kappa_3\kappa},\quad \zeta=\frac{\kappa^2-\kappa_1^2}{\kappa_3\kappa},\quad \xi=\frac{\kappa^2-\kappa_2^2}{\kappa_3\kappa}.$$

When $\kappa_3=0$,

$$\hat{u}_j(\boldsymbol{\kappa},t)=\hat{u}_j(\boldsymbol{\kappa},0),\quad \hat{\theta}(\boldsymbol{\kappa},t)=\hat{\theta}(\boldsymbol{\kappa},0)-S_\theta\hat{u}_3(\boldsymbol{\kappa},0)t, \tag{8}$$

where κ_i is the wave number of the i-th direction. The RDT solution for the velocity field is also obtained by Bartello *et al.*[21] From the above equations, it is found that the tem-

Downloaded 06 Sep 2010 to 133.68.192.96. Redistribution subject to AIP license or copyright; see http://pof.aip.org/about/rights_and_permissions

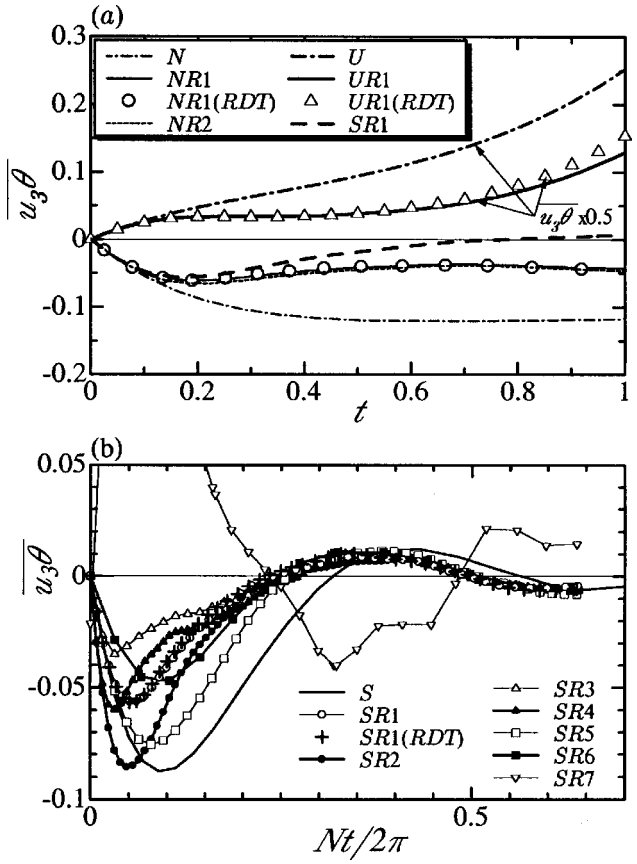

FIG. 2. The time evolution of $\overline{u_3\theta}$; (a) Cases N, NR1, NR2, UR1, U, SR1; (b) Cases S, SR1–7

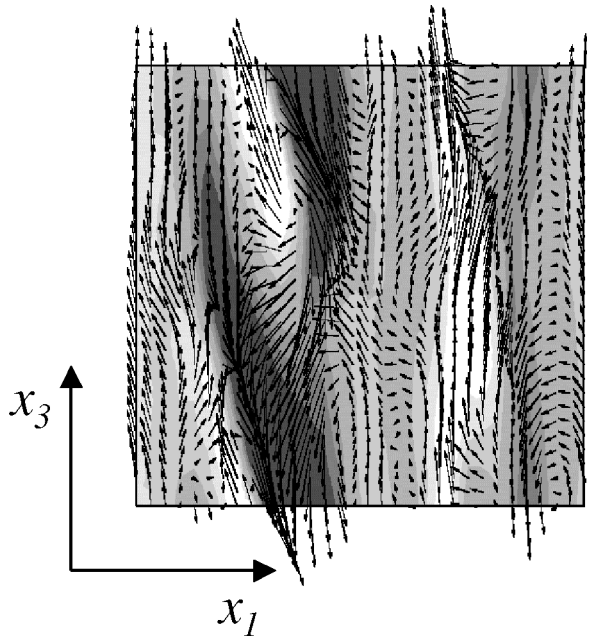

FIG. 3. Distributions of the temperature fluctuation and velocity vectors in the x_1-x_3 plane (Case UR1): Black to white; -1.8 to 1.8, $t=2.0$.

perature fluctuations associated with the $\kappa_3=0$ mode should increase linearly, while the fluctuations at other wave numbers oscillate and fail to develop. Thus, the temperature fluctuations should become independent in the x_3 direction, and hence become two-dimensional when the flow develops sufficiently.

In the following, the effects of two-dimensionalization of the temperature fluctuations are discussed, especially in the cases of stable and unstable stratification. Figures 2(a) and (b) show the time evolution of the vertical turbulent heat flux $\overline{u_3\theta}$. In Fig. 2(b), the time t is nondimensionalized by the Brunt–Väisälä frequency $N=\sqrt{g\beta S_\theta}$. The magnitude of $\overline{u_3\theta}$ increases from zero in all cases because of the mean temperature gradient imposed vertically. However, in the neutrally stratified case with solid rotation (NR), the increase of the magnitude of $\overline{u_3\theta}$ is markedly smaller than in the case with no solid rotation (N). This must be because the temperature fluctuations are transported vertically only through the velocity fluctuations of the lowest wave number, i.e., $\kappa_3=0$. In both stably and unstably stratified cases (SR and UR), this effect of the rotation is clearly observed in the developing period of turbulent heat flux.

From Fig. 2(b), it is also found that in the stable stratification with rotation (SR), $\overline{u_3\theta}$ oscillates at nearly twice the Brunt–Väisälä frequency $2N$, while the oscillation period becomes larger in the case without rotation (S).

In the case of stable and unstable stratification, the following equation is obtained for the vertical velocity component u_3 by neglecting nonlinear and diffusion terms:

$$\frac{\partial^2}{\partial t^2}\nabla^2 u_3+4\Omega^2\frac{\partial^2 u_3}{\partial x_3^2}+N^2\left(\frac{\partial^2 u_3}{\partial x_1^2}+\frac{\partial^2 u_3}{\partial x_2^2}\right)=0, \tag{9}$$

which equation is derived by differentiating the equation of $\nabla^2 u_3$ with respect to time and eliminating temperature fluctuation θ by using the equation for θ, i.e., $\partial\theta/\partial t=-S_\theta u_3$. Detailed information on how to derive Eq. (9) is available in the literature.[25] The Fourier spectrum of u_3, i.e., $\hat{u}_3$, should oscillate at the following frequency, f, under stable stratification because N^2 takes a positive value:

$$f=\sqrt{\frac{N^2(\kappa_1^2+\kappa_2^2)+4\Omega^2\kappa_3^2}{\kappa_1^2+\kappa_2^2+\kappa_3^2}}. \tag{10}$$

The temperature fluctuations also oscillate at this frequency f when both the nonlinear and diffusive terms are neglected. Considering that the temperature fluctuations in the region of $\kappa_3=0$ become dominant when the rotation is imposed, the characteristic frequencies of the temperature and vertical velocity fluctuation ultimately become the Brunt–Väisälä frequency N. Accordingly, the correlation between them, or the product of θ and u_3, should oscillate at twice the Brunt–Väisälä frequency $2N$ as shown in Fig. 2(b).

B. Effects of rotation on unstably stratified turbulence

Figure 3 shows distributions of the temperature fluctuation and velocity vectors in the x_1-x_3 plane in the unstably stratified case with rotation. The temperature fluctuations in this case also become approximately two-dimensional, as in the neutrally stratified case with rotation. However, in this case, the fluids move upward in the regions of positive temperature fluctuations, while they move downward when the

Downloaded 06 Sep 2010 to 133.68.192.96. Redistribution subject to AIP license or copyright; see http://pof.aip.org/about/rights_and_permissions

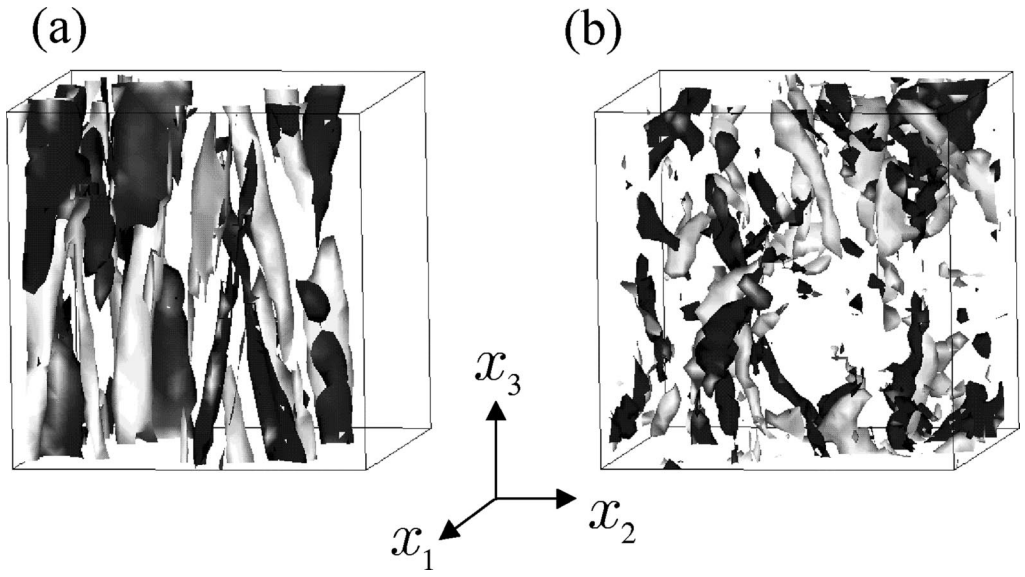

FIG. 4. Iso-surfaces of ω_3 at $t=2.0$. White iso-surfaces represent $\omega_3/\omega_{3rms}=2.0$ while black iso-surfaces are $\omega_3/\omega_{3rms}=-2.0$; (a) Case UR1; (b) Case U.

temperature fluctuations take negative values. It should also be noted that both the upward and downward motions are twisted in the spanwise direction.

Figures 4(a) and (b) show the iso-surfaces of the vertical component of the vorticity ω_3 in the case of the unstable stratification with and without rotation, respectively. Under the unstable stratification with rotation, the vortex columns of ω_3 are clearly observed to be elongated in the direction parallel to the axis of rotation. However, in cases without rotation or unstable stratification (not shown here), no elongated vortex columns are generated. In addition, in the calculation using the RDT, though the figure is not shown here, the vortex columns are not formed regardless of the initial condition, thus indicating that the nonlinear effects are absolutely required to generate the vortex columns.

Figures 5(a) and (b) show the joint probability density function (p.d.f.) between the vertical vorticity ω_3 and the pressure fluctuation p in Cases UR1 and U, respectively. In Case UR1, the large positive vertical vorticity is indeed most likely associated with the large negative pressure fluctuation, whereas the large negative vertical vorticity is associated with the large positive pressure fluctuation. Thus, the observed vortex columns are generated under the geostrophic balance between the pressure gradient and the Coriolis force. In the case without rotation, both large positive and negative vertical vorticities tend to be associated with negative pressure fluctuations.

Next, we investigate the generation of the vertical vorticity in more detail. The equation of the vertical vorticity ω_3 is given as follows:

$$\frac{\partial \omega_3}{\partial t}+u_j\frac{\partial \omega_3}{\partial x_j}=\omega_3\frac{\partial u_3}{\partial x_3}+2\Omega\frac{\partial u_3}{\partial x_3}+\left(\frac{\partial u_3}{\partial x_2}\frac{\partial u_1}{\partial x_3}-\frac{\partial u_3}{\partial x_1}\frac{\partial u_2}{\partial x_3}\right)+\nu\frac{\partial^2 \omega_3}{\partial x_j \partial x_j}. \tag{11}$$

In Eq. (11), the first and second terms on the right-hand side represent the nonlinear and linear vortex-stretching terms, respectively. Figures 6(a) and (b) show the joint p.d.f. between the vertical vorticity ω_3 and the strain rate $\partial u_3/\partial x_3$ in Cases UR1 and U, respectively. In Case U, large plus and minus vertical vorticities are mainly associated with the intensive $\partial u_3/\partial x_3$ with a positive sign. This indicates that the vertical vorticity is generated mostly by the nonlinear term $\omega_3(\partial u_3/\partial x_3)$ in Eq. (11). On the other hand, in Case UR1 where vortex columns of ω_3 are clearly observed, the large

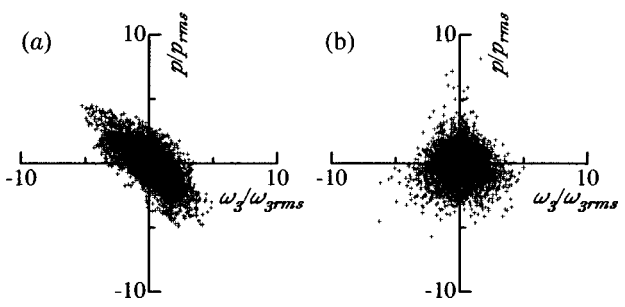

FIG. 5. (a) The joint p.d.f. between pressure p and vertical vorticity ω_3; (a) Case UR1, $t=2.0$; (b) Case U, $t=2.0$.

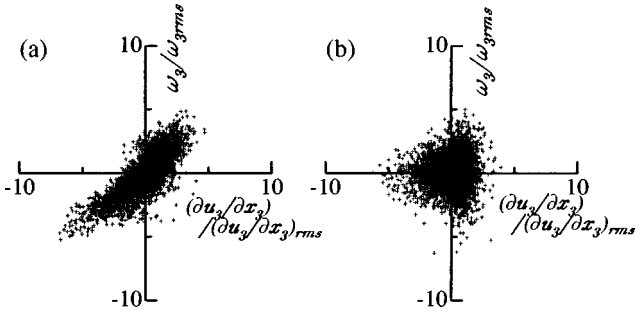

FIG. 6. The joint p.d.f. between vertical vorticity ω_3 and $\partial u_3/\partial x_3$; (a) Case UR1, $t=2.0$; (b) Case U, $t=2.0$.

Downloaded 06 Sep 2010 to 133.68.192.96. Redistribution subject to AIP license or copyright; see http://pof.aip.org/about/rights_and_permissions

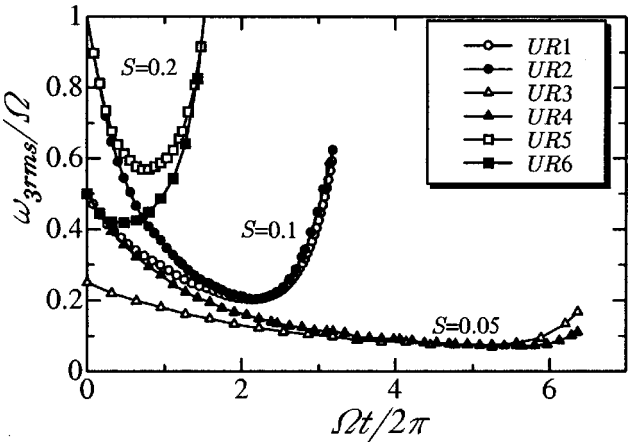

FIG. 7. The time evolution of ω_3 in Cases UR1–6.

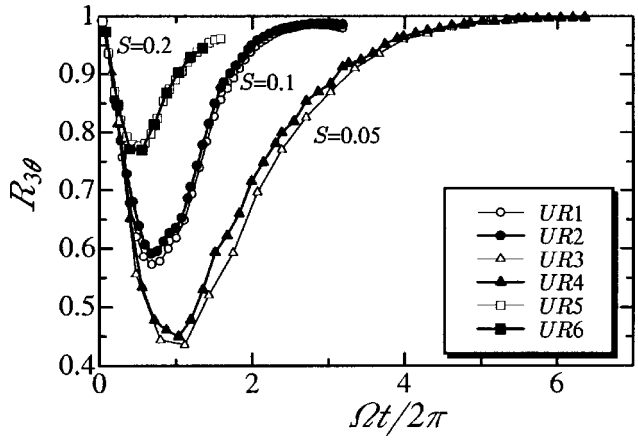

FIG. 8. The time evolution of the cross-correlation between vertical velocity and temperature fluctuations in Cases UR1–6.

ω_3 is indeed most likely associated with the large $\partial u_3/\partial x_3$ with the same signs as ω_3. Thus, the observed vortex columns of ω_3 must be generated by the vortex stretching associated with the linear term $2\Omega(\partial u_3/\partial x_3)$.

The generation mechanism of vortex columns can be explained by using the equation on a potential vorticity, defined as

$$\pi=(\boldsymbol{\omega}+2\boldsymbol{\Omega})\cdot\boldsymbol{\nabla}\tilde{\rho}=\beta(\boldsymbol{\omega}+2\boldsymbol{\Omega})\cdot\boldsymbol{\nabla}(\Theta+\theta) \tag{12}$$

$$=\beta\left(\omega_3 S_\theta+\boldsymbol{\omega}\cdot\boldsymbol{\nabla}\theta+2\Omega S_\theta+2\Omega\frac{\partial\theta}{\partial x_3}\right), \tag{13}$$

where $\tilde{\rho}$ is nondimensionalized density and the boldface type represents a vector. In the above equation, $\boldsymbol{\omega}\cdot\boldsymbol{\nabla}\theta$ can be neglected because Ω and Θ are sufficiently large in comparison to $\boldsymbol{\omega}$ and θ, respectively. Then, from the conservation law of a potential vorticity,[25] the following equation is obtained:

$$\frac{D\pi}{Dt}=\beta S_\theta\left(\frac{D\omega_3}{Dt}+\frac{D}{Dt}\left(\frac{2\Omega}{S_\theta}\frac{\partial\theta}{\partial x_3}\right)\right)=0. \tag{14}$$

It should also be noted that ω_3 and $(2\Omega/S_\theta)\partial\theta/\partial x_3$ represent barotropic and baroclinic vorticities, respectively.

Because the nonlinear terms included in an equation of the temperature fluctuation θ were not required to generate vortex columns (not shown here), the time derivative of $\partial\theta/\partial x_3$ can be approximated as

$$\frac{D}{Dt}\frac{\partial\theta}{\partial x_3}=-S_\theta\frac{\partial u_3}{\partial x_3}. \tag{15}$$

Then, the time derivative of a potential vorticity should satisfy

$$\beta S_\theta\left(\frac{D\omega_3}{Dt}-2\Omega\frac{\partial u_3}{\partial x_3}\right)=0. \tag{16}$$

This result indicates that the vortex columns are generated in the process by which the baroclinic vorticity is transformed into the barotropic vorticity, which mechanism can be represented by the linear vortex-stretching term [see Eq. (11)].

Figure 7 shows the time evolution of the r.m.s. value of the vertical vorticity ω_3 in Cases UR1–6, where both ω_3 and t are nondimensionalized by the imposed rotation rate Ω. The parameter S given in Fig. 7 is the ratio of the Brunt–Väisälä frequency to the angular frequency of rotation. In the case of unstable stratification ($S_\theta<0$), S is defined as

$$S\equiv\frac{\sqrt{|g\beta S_\theta|}}{2\Omega}. \tag{17}$$

As shown in Table I, the value of S increases from 0.05 to 2.0 in Cases UR1 to UR6 and UR7 to UR12. In the cases with the same value of S, it can be seen from Fig. 7 that the vertical vorticity begins to increase at the same normalized time $\Omega t/2\pi$, and its time evolutions almost coincide with each other. This indicates that the vortical structure of unstably stratified rotating turbulence is almost entirely determined by the parameters S and Ω associated with the body force terms. Our results are interestingly similar to the experiments of injecting dense salty water into the rotating tank, where the evolution of the vortex columns is determined by the parameter S.[15] It is also found that the small S, i.e., smaller effects of buoyancy than the Coriolis force, does delay the increase in ω_3.

The corresponding time evolution of the cross-correlation of u_3 and θ is presented in Fig. 8. Initially, the cross-correlation $R_{3\theta}$ decreases due to the effects of rotation, then begins to increase almost up to unity under the effects of rotation. Figures 9 and 10 show the time evolution of ω_3 and $R_{3\theta}$ in Cases UR7 to UR12, respectively. Their time evolutions are qualitatively similar to those observed in the cases with the initial integral scale (UR1–6). This should be because even if the initial integral scales are set to be zero as in UR7–12, the imposed rotation enhances the backscatter of the energy cascade and increases the integral scale in the x_3 direction.[19–21] This mechanism is thought to be a prelude to a Taylor–Proudmann reorganization into two-dimensional turbulence,[19] although the present generation mechanism of vortex columns itself is not due to the Taylor–Proudmann theory, but directly related to the above-mentioned vortex stretching in the vertical direction. In the cases without the integral scale, more time is needed to generate vortex columns.

Comparison of Figs. 8 and 10 with Figs. 7 and 9 reveals that ω_3 begins to increase when $R_{3\theta}$ has reached almost

Downloaded 06 Sep 2010 to 133.68.192.96. Redistribution subject to AIP license or copyright; see http://pof.aip.org/about/rights_and_permissions

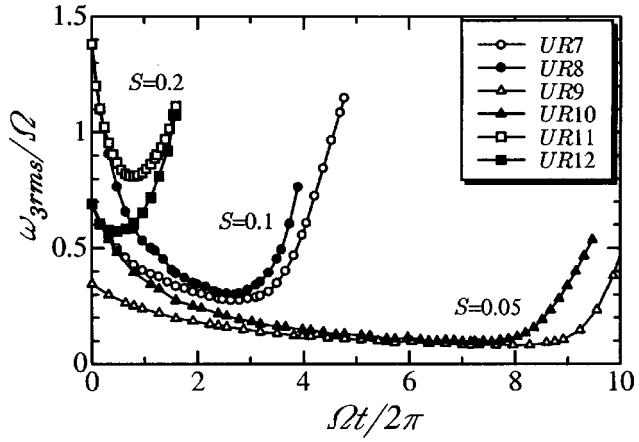

FIG. 9. The time evolution of ω_3 in Cases UR7–12.

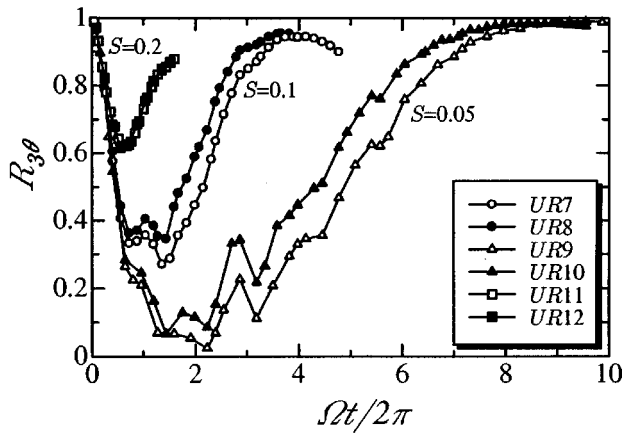

FIG. 10. The time evolution of the cross-correlation between vertical velocity and temperature fluctuations in Cases UR7–12.

unity, indicating that the vortical structures begin to emerge after both temperature and velocity fluctuations become two-dimensional.

Figure 11 shows the vertical structure of temperature and velocity vectors, while Fig. 12 shows the iso-surfaces of ω_3. Symbols (a) and (b) appended to the figures represent the cases of $S=0.1$ and 0.05, respectively. These figures are the snapshots at the instance when spatially averaged vertical vorticity begins to increase, as shown in Figs. 7 and 9. It is noted from Fig. 11 that both temperature and velocity fluctuations tend to be aligned in the vertical direction, and become almost two-dimensional. It is also found that the vortex columns as observed in Fig. 4(a) begin to emerge in both cases of $S=0.05$ and 0.1.

C. Effects of the nonlinear term

The effects of the nonlinear term on the generation mechanisms of vortex columns should be discussed. Figure 13 shows the time evolution of Reynolds normal stresses in Cases U and UR1. After the initial period of decaying, both $\overline{u_1^2}$ and $\overline{u_2^2}$ in Case UR1 begin to increase remarkably at $t \simeq 1.7$, while in Case U an increase in $\overline{u_1^2}$ and $\overline{u_2^2}$ occurs gradually from a much earlier time of $t=0.8$. In Case UR1, the increase of $\overline{u_3^2}$ is also delayed in comparison to Case U. Thus, the increase of velocity fluctuations due to the effect of unstable stratification is delayed by imposing rotation. Interestingly, in the RDT for Case UR1, neither $\overline{u_1^2}$ nor $\overline{u_2^2}$ increases during all the period of the calculation, although the time evolution of $\overline{u_3^2}$ almost agrees with the result of DNS. Therefore, the increase of both $\overline{u_1^2}$ and $\overline{u_2^2}$, which should be associated with the occurrence of horizontal eddies, results from the effects of the nonlinear term, whereas the increase of $\overline{u_3^2}$ relates mainly to the linear term. Figure 14 shows the time evolution of the r.m.s. value of the strain rate $\partial u_3/\partial x_3$. The difference is clearly observed between RDT and DNS for Case UR1 after the time t becomes 1.7. We also find that

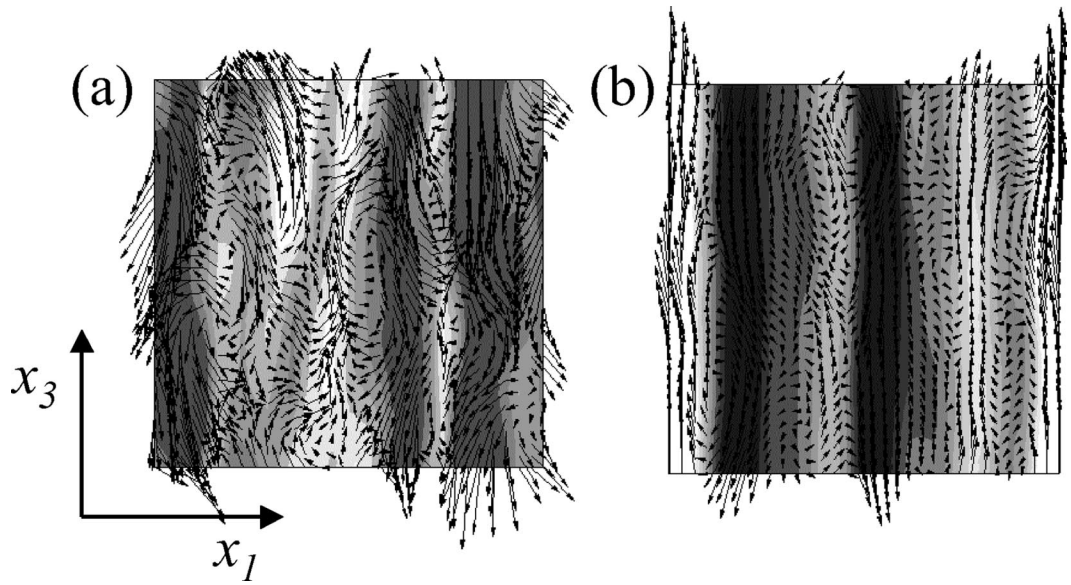

FIG. 11. The vertical structures of temperature fluctuations and velocity vectors in the (x_1,x_3) plane at the instance when the vertical vorticity ω_3 begins to increase; (a) Case UR7, $\Omega t/2\pi=3.98$, black to white: $\theta=-2.5$ to 2; (b) Case UR10, $\Omega t/2\pi=8.75$, black to white: $\theta=-5$ to 4.

Downloaded 06 Sep 2010 to 133.68.192.96. Redistribution subject to AIP license or copyright; see http://pof.aip.org/about/rights_and_permissions

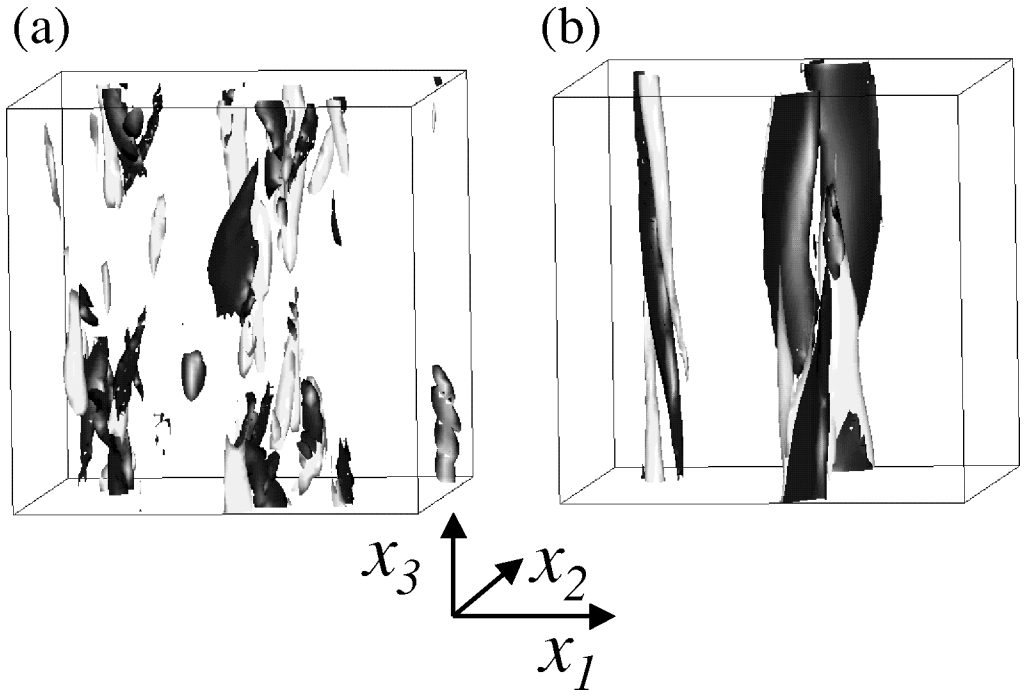

FIG. 12. The iso-surfaces of vorticity ω_3 at the instance when the vertical vorticity ω_3 begins to increase. Black iso-surfaces represent $\omega_3/\omega_{3rms}=-2.5$ while white iso-surfaces are $\omega_3/\omega_{3rms}=2.5$; (a) Case UR7, $\Omega t/2\pi=3.98$; (b) Case UR10, $\Omega t/2\pi=8.75$.

the time evolution of both $\overline{u_1^2}$ and $\overline{u_2^2}$ is closely associated with that of $\overline{(\partial u_3/\partial x_3)^2}$, i.e., the increase of these quantities begins almost at the same time. These results shown in Figs. 13 and 14 support our supposition that the elongated vortex columns are generated by the vortex stretching term associated with the externally imposed rotation and the strain rate $\partial u_3/\partial x_3$.

Figures 15(a) and (b) show the energy spectra of the vertical velocity and vorticity, respectively. It is useful to divide the energy spectrum into two parts: one in the region where the wave numbers satisfy the following formula:

$$f^2=\frac{N^2(\kappa_1^2+\kappa_2^2)+4\Omega^2\kappa_3^2}{\kappa_1^2+\kappa_2^2+\kappa_3^2}<0,$$

the other in the region where the wave numbers satisfy $f^2>0$. The importance of this criterion for the sign of f^2 can be found by analytically solving the equations of RDT as shown in the following:

• $f^2>0$,

$$\hat{u}_3(\boldsymbol{\kappa},t)=\hat{u}_3(\boldsymbol{\kappa},0)\cos ft+\frac{2\Omega\kappa_3}{f\kappa^2}\{\kappa_2\hat{u}_1(\boldsymbol{\kappa},0)-\kappa_1\hat{u}_2(\boldsymbol{\kappa},0)\}\sin ft,$$

$$\hat{\theta}(\boldsymbol{\kappa},t)=-S_\theta\frac{\hat{u}_3(\boldsymbol{\kappa},0)}{f}\sin ft+\frac{2\Omega\kappa_3}{f^2\kappa^2}S_\theta\{\kappa_2\hat{u}_1(\boldsymbol{\kappa},0)-\kappa_1\hat{u}_2(\boldsymbol{\kappa},0)\}(\cos ft-1); \quad (18)$$

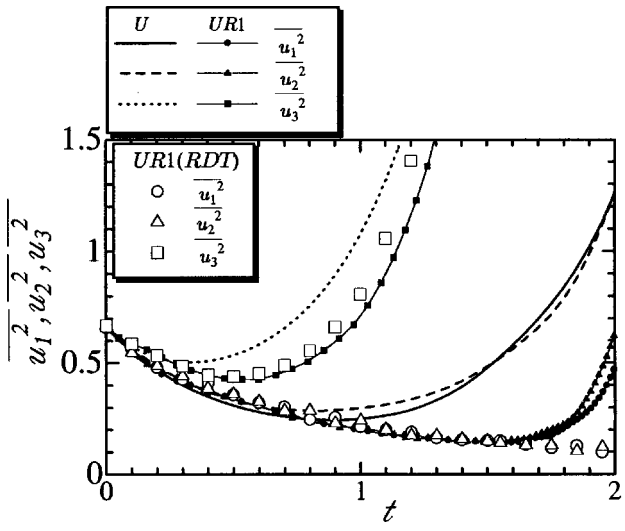

FIG. 13. The time evolution of Reynolds stresses in Cases U and UR1.

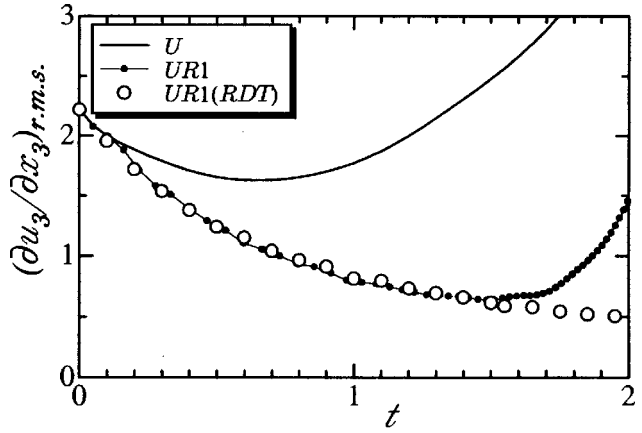

FIG. 14. The time evolution of the r.m.s. value of strain rate $\partial u_3/\partial x_3$ in Cases U and UR1.

Downloaded 06 Sep 2010 to 133.68.192.96. Redistribution subject to AIP license or copyright; see http://pof.aip.org/about/rights_and_permissions

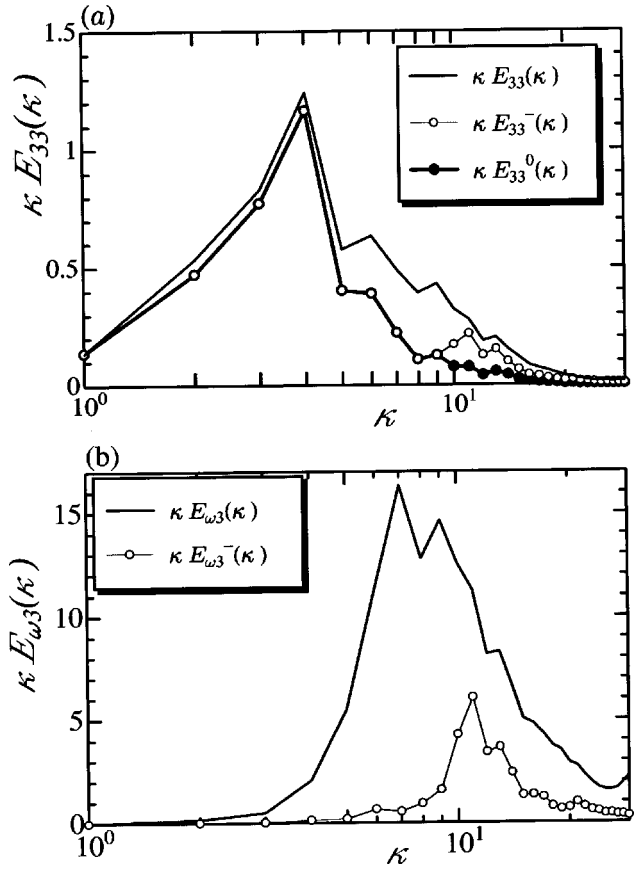

FIG. 15. The energy spectra in Case UR7 at the instance $\Omega t/2\pi=3.98$. The superscripts 0 and $-$ represent energy in the region $\kappa_3=0$ and $f^2<0$, respectively; (a) the energy spectra of vertical velocity; (b) the energy spectra of vertical vorticity.

• $f^2<0$,

$$\hat{u}_3(\boldsymbol{\kappa},t)=\hat{u}_3(\boldsymbol{\kappa},0)\cosh ft+\frac{2\Omega\kappa_3}{f\kappa^2}\{\kappa_2\hat{u}_1(\boldsymbol{\kappa},0)-\kappa_1\hat{u}_2(\boldsymbol{\kappa},0)\}\sinh ft,$$

$$\hat{\theta}(\boldsymbol{\kappa},t)=-S_\theta\frac{\hat{u}_3(\boldsymbol{\kappa},0)}{f}\sinh ft+\frac{2\Omega\kappa_3}{f^2\kappa^2}S_\theta\{\kappa_2\hat{u}_1(\boldsymbol{\kappa},0)-\kappa_1\hat{u}_2(\boldsymbol{\kappa},0)\}(\cosh ft-1); \tag{19}$$

$\kappa_3=0$,

$$\hat{u}_3(\boldsymbol{\kappa},t)=\hat{u}_3(\boldsymbol{\kappa},0)\cosh Nt,$$

$$\hat{\theta}(\boldsymbol{\kappa},t)=-S_\theta\frac{\hat{u}_3(\boldsymbol{\kappa},0)}{N}\sinh Nt. \tag{20}$$

As is evident in the above formulas, without nonlinear terms, both the temperature and vertical velocity spectra increase in the region where f^2 takes a negative value, while they fail to develop in the positive f^2 region. One should also note that in the region of $\kappa_3=0$, the time evolution of both the vertical velocity and the temperature field is only dependent on the Brunt–Väisälä frequency, and thus determined only by buoyancy.

In Fig. 15(a), almost all vertical energy is contained in the region $f^2<0$, suggesting that it is possible to predict the increase of $\overline{u_3^2}$ without the nonlinear term [see Eq. (19)]. It is also found that the energy satisfying $f^2<0$ is, at the same time, located in the region $\kappa_3=0$. However, around $\kappa=8$, E_{33} increases in the positive f^2 region where κ_3 takes a nonzero value, and thus contributes to the increase of $\partial u_3/\partial x_3$.

On the other hand, the energy spectrum of ω_3 shown in Fig. 15(b) is almost in the region $f^2>0$, and concentrated around $\kappa=8$ where the energy of $\overline{u_3^2}$ in the region $f^2>0$ increases, indicating that the vertical velocity fluctuations satisfying $f^2>0$ contribute to the generation of the vortex columns through the linear vortex stretching. Thus, the role of the nonlinear term is to increase u_3 at the nonzero value of κ_3 due to the cascade-type energy transfer from the lower to higher wave numbers, which should interrupt oscillation of vertical velocity fluctuations in the region $f^2>0$ and enhance their magnitude. This energy cascade should be enhanced by buoyancy force as suggested recently by Komori and Nagata.[22]

When f^2 takes a positive value, the following relation is obtained between horizontal and vertical wave numbers associated with vortex columns:

$$\frac{2\pi}{\sqrt{\kappa_1^2+\kappa_2^2}}>\frac{2\pi}{\kappa_3}S.$$

The right-hand side of the equation, i.e., $2\pi S/\kappa_3$, represents the internal Rossby radius of deformation. Thus, in the generated vortex columns their horizontal length scale must be larger than the Rossby radius of deformation. This indicated that the Coriolis force directly affects the horizontal structures of vortex and geostrophic balance is pertained, although their vertical structure should be determined only by a buoyancy force.

IV. CONCLUSIONS

By using both direct numerical simulation and rapid distortion theory, the following conclusions are established pertaining to the geostrophic flow under density stratification. In the neutrally stratified case with rotation, the heat transfer occurs in the direction of a rotational axis. Thus, the isosurfaces of the temperature fluctuations are aligned in the direction parallel to the axis of rotation, and become very close to two-dimensional. In the stably stratified case with rotation, the velocity and temperature fluctuations oscillate with the Brunt–Väisälä frequency. In the unstably stratified case with rotation, the elongated vortex columns are generated in the direction parallel to the axis of rotation. These vortex columns are generated by the effect of linear vortex stretching associated with the externally imposed rotation Ω and strain rate $\partial u_3/\partial x_3$. The linear vortex stretching is closely associated with the process of energy conversion from baroclinic vorticity to barotropic vorticity. RDT cannot generate the vortex columns, because the nonlinear term is required to suppress the oscillation and enhance the magnitude of the strain rate $\partial u_3/\partial x_3$.

It is also found that the time evolution of vortex columns is determined by the parameter representing the ratio of the

Downloaded 06 Sep 2010 to 133.68.192.96. Redistribution subject to AIP license or copyright; see http://pof.aip.org/about/rights_and_permissions

Brunt–Väisälä frequency to the angular frequency of rotation. The vortex columns begin to emerge when both the velocity and temperature fluctuations become two-dimensional, and their cross-correlation becomes almost unity. The horizontal length scale of the vertical vortex becomes larger than the Rossby radius of deformation. Thus, the Coriolis force directly affects the horizontal structures of the vortex, although their vertical structure should be determined by the buoyancy force.

[1]Y. Nakagawa and P. Frenzen, ''A theoretical and experimental study of cellular convection in rotating fluids,'' Tellus **7**, 1 (1955).
[2]H. T. Rossby, ''A study of Bénard convection with and without rotation,'' J. Fluid Mech. **36**, 309 (1969).
[3]F. H. Busse and K. E. Hikes, ''Convection in a rotating layer: A simple case of turbulence,'' Science **208**, 173 (1980).
[4]B. M. Boubnov and G. S. Golitsyn, ''Experimental study of convective structures in rotating fluids,'' J. Fluid Mech. **167**, 503 (1986).
[5]B. M. Boubnov and G. S. Golitsyn, ''Temperature and velocity field regimes of convective motions in a rotating plane fluid layer,'' J. Fluid Mech. **219**, 215 (1990).
[6]H. J. S. Fernando, D. L. Boyer, and R-R. Chen, ''Turbulent thermal convection in rotating and stratified fluids,'' Dyn. Atmos. Oceans **13**, 95 (1989).
[7]H. J. S. Fernando, R-R. Chen, and D. L. Boyer, ''Effects of rotation on convective turbulence,'' J. Fluid Mech. **228**, 513 (1991).
[8]S. Sakai, ''The horizontal scale of rotating convection in the geostrophic regime,'' J. Fluid Mech. **333**, 85 (1997).
[9]S. Raasch and D. Etling, ''Numerical simulation of rotating turbulent thermal convection,'' Beitr. Phys. Atmosph. **64**, 185 (1991).
[10]W. Cabot, O. Hubickyj, J. B. Pollack, and P. Cassen, ''Direct numerical simulations of turbulent convection: I. Variable gravity and uniform rotation,'' Geophys. Astrophys. Fluid Dyn. **53**, 1 (1990).
[11]K. Julien, S. Legg, J. McWilliams, and J. Werne, ''Hard turbulence in rotating Rayleigh–Bénard convection,'' Phys. Rev. E **53**, 5557 (1996).
[12]K. Julien, S. Legg, J. McWilliams, and J. Werne, ''Rapidly rotating turbulent Rayleigh–Bénard convection,'' J. Fluid Mech. **322**, 243 (1996).
[13]H. Jones and J. Marshall, ''Convection with rotation in a neutral ocean: A study of open-ocean deep convection,'' J. Phys. Oceanogr. **23**, 1009 (1993).
[14]T. Maxworthy and S. Narimousa, ''Unsteady, turbulent convection into a homogeneous, rotating fluid, with oceanographic applications,'' J. Phys. Oceanogr. **24**, 865 (1994).
[15]K. R. Helfrich, ''Thermals with background rotation and stratification,'' J. Fluid Mech. **259**, 265 (1994).
[16]K. G. Speer, ''A forced baroclinic vortex around a hydrothermal plume,'' Geophys. Res. Lett. **16**, 461 (1989).
[17]J. Bardina, J. H. Ferziger, and R. S. Rogallo, ''Effect of rotation on isotropic turbulence: Computation and modelling,'' J. Fluid Mech. **154**, 321 (1985).
[18]L. Jacquin, O. Leuchter, C. Cambon, and J. Mathieu, ''Homogeneous turbulence in the presence of rotation,'' J. Fluid Mech. **220**, 1 (1990).
[19]N. N. Mansour, C. Cambon, and C. G. Speziale, ''Theoretical and computational study of rotating isotropic turbulence,'' in *Studies in Turbulence*, edited by T. B. Gatski, S. Sarker, and C. G. Speziale (Springer-Verlag, Berlin, 1992), pp. 59–75.
[20]N. N. Mansour, C. Cambon, and C. G. Speziale, ''Single point modelling of initially isotropic turbulence under uniform rotation,'' in *Annual Research Briefs*, Center for Turbulence Research, NASA–Ames Research Center—Stanford University, 1991, pp. 159–167.
[21]P. Bartello, O. Metais, and M. Lesieur, ''Coherent structures in rotating three-dimensional turbulence,'' J. Fluid Mech. **273**, 1 (1994).
[22]S. Komori and K. Nagata, ''Effects of unstable stratification and mean shear on the chemical reaction in grid-generated turbulence,'' in *Proceedings of the 11th Symposium on Turbulent Shear Flows*, Grenoble, France, 1997, Vol. 2, pp. 21.25–21.27.
[23]J. C. McWilliams, ''Statistical properties of decaying geostrophic turbulence,'' J. Fluid Mech. **198**, 199 (1989).
[24]J. C. McWilliams, J. B. Weiss, and I. Yavneh, ''Anisotropy and coherent vortex structures in planetary turbulence,'' Science **264**, 410 (1994).
[25]M. Lesieur, *Turbulence in Fluids* (Kluwer Academic, The Netherlands, 1990).
[26]O. Metais, P. Bartello, E. Garnier, J. J. Riley, and M. Lesieur, ''Inverse cascade in stably stratified rotating turbulence,'' Dyn. Atmos. Oceans **23**, 193 (1996).
[27]A. E. Gill, *Atmosphere–Ocean Dynamics* (Academic, New York, 1982).

Downloaded 06 Sep 2010 to 133.68.192.96. Redistribution subject to AIP license or copyright; see http://pof.aip.org/about/rights_and_permissions